Microstructure evolution during dynamic recrystallisation in polycrystalline nickel superalloys

E.I. Galindo-Nava*, C.M.F. Rae

Department of Materials Science and Metallurgy, University of Cambridge, United Kingdom

27 Charles Babbage Rd, Cambridge, CB3 0FS, UK

*email: eg375@cam.ac.uk

+44 1223 334300

Abstract

A new theory for describing grain structure evolution during discontinuous dynamic recrystallisation in nickel–based superalloys is presented. The evolution of the average and recrystallised grain size is determined during dynamic straining and at steady state by computing the variation in the number of grains with strain. The initial grain size distribution is combined with a size distribution function containing recrystallised grains only; subsequent evolution depends on their respective average values. This allows us to deconvolute the recrystallised and deformed grain distributions to obtain the recrystallised volume fraction. Precipitation pinning and solute drag are incorporated in the model by measuring the fractional loss of stored energy when a boundary encounters such defects depending on how they accumulate at the boundary. The model results are validated against data from eleven polycrystalline superalloys, covering a wide range in composition, initial microstructure and deformation regime.

Keywords: Recrystallization; grain growth; grain refinement; nickel based superalloys; plasticity; forging

1 Introduction

Polycrystalline Ni-based superalloys are widely employed in industries such as aerospace, energy, nuclear, maritime and petrochemical, due to their excellent mechanical properties combined with good corrosion resistance at high temperatures [1]. A number of precipitation strengthening mechanisms are introduced to produce this high performance during in-service conditions. However, crucial mechanical properties such as tensile strength, creep resistance and low-cycle fatigue remain highly sensitive to the alloy grain structure via both the average and the distribution of grain size [2]. The latter is manipulated during thermomechanical processing at high temperatures, by hot-forging and annealing treatments [1].

Dynamic recrystallisation (DRX) is the principal mechanism for tailoring specific grain structures during hot forming: it can be controlled by modifying both the deformation conditions and the initial microstructure. A number of coarser precipitates are introduced, such as carbides, cubic coherent γ' (Ni_3(Al-Ti)) and the orthorhombic incoherent δ (Ni_3Nb) intermetallics, to obtain a finer grain size by inhibiting recrystallisation and grain growth. Moreover, solute drag from the many alloying elements, affects both the flow stress of the material and the recrystallisation, increasing the complexity of unraveling the individual elemental contributions to grain refinement. The focus on experimental characterisation during the hot deformation of polycrystalline superalloys[3, 4, 5, 6, 7, 8, 9, 10, 11, 12, 13, 14, 15, 16] is perhaps indicative of the lack of physics-based theoretical descriptions able to predict grain structure evolution as a function of wide variations in composition and deformation conditions [17]. For the most part technologists rely on semi-empirical or phenomenological algorithms, where properties are related to a limited number of parameters representing specific deformation conditions and composition. This impedes extending their application to novel scenarios. Thus, deriving a fundamental approach that quantifies individual contributions to grain refinement under a wide process window serves not only to optimise current alloy performance, but can also aid our understanding of the underlying mechanisms and

assist in developing new alloys and synergistic processing regimes.

The objective of this work is to introduce a novel modelling approach for describing grain structure evolution during dynamic recrystallisation and to validate this in eleven polycrystalline superalloys. A number of features are described: 1) the average ($\overline{D}$) and recrystallised (D_{DRX}) grain size during straining and at steady state, where grain nucleation and growth effects are considered, 2) the grain size distribution, 3) grain number density, and 4) recrystallised volume fraction evolution during straining. It is demonstrated that the previous features can be fully characterised by describing the evolution of $\overline{D}$ and D_{DRX} only. The effects of solute drag, particle pinning and processing condition are incorporated in this model. Grain size has previously been modelled for Ni–binary alloys (Item 1), including solute drag effects [18]; this work extends this to multicomponent alloys containing seven substitutional and one interstitial elements. An alternative approach for particle pinning effects on grain growth is proposed and is shown to depend on the average particle spacing, volume fraction, average size and morphology.

2 Materials and deformation conditions

Table 1 shows the chemical composition of the commercial alloys referred to in this work. They cover a wide compositional range in seven of the substitutional elements and interstitial carbon; contributions from other substitutional elements are neglected.

Table 1: Materials employed in this work. Chemical composition is displayed in wt%.

No.	Alloy	Cr	Fe	Nb	Co	Mo	Al	Ti	C
1	AllVac 718	17.65	20.98	5.7	0.25	2.9	0.52	0.94	0.019
2	Inconel 625	21.32	0.11	3.73	0	8.58	0.18	0.16	0.053
3	Inconel Age 625	21.1	5.08	3.39	0	8.06	0.2	1.35	0.007
4	Pyromet 625	21.9	2.38	3.96	0	8.84	0.18	0.25	0.042
5	Inconel 690	28.88	10.05	0	0	0	0.18	0.29	0.038
6	Inconel 718	18.1	18.3	5.5	0.37	3.05	0.49	0.98	0.03
7	Inconel 740H	25	0	2	20	0.5	1.5	1.5	0.03
8	Nimonic 75	19.5	0	0	16.5	0	1.5	2.5	0.027
9	Nimonic 80A	19.54	0.21	0	0	0	1.5	2.4	0.07
10	Nimonic 90	19.5	0	0	16.5	0	1.5	2.5	0.07
11	Nimonic 105	15	0	0	0	5	4.7	1.2	0.13

Table 2 shows the deformation conditions and initial microstructure for these alloys, where D_0 is the initial grain size, ε and $\dot{\varepsilon}$ are the axial strain and strain rate, respectively; the experimental measurements were obtained from the literature. In most cases, the average or recrystallised grain size was reported at large strains only. For Nimonic 75, 90 and 105, no initial grain size was reported and the measured values were assumed to have reached steady state (D_{ss}). The effect of precipitates such as $M_{23}C_6$ and δ are considered in this work. Table 2 shows the $M_{23}C_6$ and δ equilibrium volume fraction F_p variation for the test temperatures, as no experimental volume fractions were reported (except for δ in two cases); the equilibrium volume fraction values were obtained from Thermocalc. Guo *et al.* [6] experimentally confirmed the presence of $M_{23}C_6$ carbides in IN 690. Carbides were experimentally observed in IN 625 and Pyromet 625, although their type was not identified; the transformation–time-

temperature diagram suggests that $M_{23}C_6$ carbides should be preserved for the duration of the test [19]. For IN 740H, the carbide volume fraction is very low and $M_{23}C_6$ only was considered to be present [13]. Although additional M_7C_3 carbides may be formed at high temperatures ($\geq$1353 K [20]) in the Nimonic series, Tian *et al.* [21] have pointed out that $M_{23}C_6$ particles are preserved at high temperatures for moderate deformation times; hence only $M_{23}C_6$ particles are analysed; this also implies that $F_{M_{23}C_6}$ at high temperatures is approximated by the volume fraction of M_7C_3 (from Thermocalc). Chaudhury and Zhao [3] measured a precipitate volume fraction less than 1% and a particle size in the range 1–15 μm in AllVac 718; however, they did not characterise the phase fraction of these particles (the heat treatment schedule was performed in the $\gamma' + \gamma'' + \delta$ region [22]). To overcome this limitation, particle pinning effects are neglected in this alloy due to the low volume fraction and large particle size, resulting in very limited pinning [23]. For δ in Inconel 718, the reported heat treatment routines were compared against the time-transformation-temperature diagram [7] to confirm whether δ is present during deformation. Only two data sets contain δ precipitates [7, 8]; other experiments do not report the presence of δ particles during deformation, consistent with the forging temperature being above the δ solvus. Moreover, experimental F_δ values are close to those prescribed by Thermocalc at equilibrium: 4% (at 1253 K) and 7% (at 1173 K), from [7] and [8] respectively, whereas from Thermocalc, the respective equilibrium fraction is 4.7% and 7.7%; hence, using the equilibrium particle volume fraction represents a good approximation. For the 625 series, no δ particles were reported in the experimental observations [5, 4].

Table 2: Deformation conditions and microstructure observation in the tested alloys.

Alloy	T (K)	$\dot{\varepsilon}$ (s^{-1})	D_0 (μm)	ε	$F_{M_{23}C_6}$ (%)	F_δ (%)	Ref.
AllVac 718	1173-1423	0.001-5	54	0.6	-	-	[3]
Inconel 625	1223-1473	0.1	81	0.7	0-1.1	-	[4]
Inconel Age 625	1223-1423	0.001-1	62	0.8	-	-	[5]
Pyromet 625	1223-1423	0.001-1	12	0.8	0.16-0.88	-	[5]
Inconel 690	1323-1473	0.01-1	42	0.7	0-0.67	-	[6]
Inconel 718	1253-1313	0.01-1.1	20	0-0.81	-	0-4.7	[7]
Inconel 718	1173-1413	0.001-1	81	0.8	-	0-7.7	[8]
Inconel 718	1273-1313	0.001-1	30-190	0.1-1.2	-	-	[9]
Inconel 718	1223-1373	0.001-0.1	176	0.7	-	-	[10]
Inconel 718	1273-1423	0.01-1.3	23-54	0.6	-	-	[11]
Inconel 718	1273-1348	0.005-0.1	114	0.7	-	-	[12]
Inconel 740H	1323-1473	0.1-1	20	0.6	0-0.12	-	[13]
Nimonic 75	1273-1473	0.1	-	0.6	0.7-1.2	-	[14]
Nimonic 80A	1223-1393	0.01-1	90	0.9	0.9-1	-	[15]
Nimonic 90	1273-1473	0.1	-	0.6	-	-	[14]
Nimonic 105	1273-1473	0.1	-	0.6	1.4-1.5	-	[14]

3 Previous theory

This section presents previous results on the nucleation of dynamic recrystallisation, grain size evolution and solute drag effects in binary Ni alloys; these concepts are further extended to polycrystalline Ni–based superalloys in the following sections.

3.1 Dynamic recrystallisation nucleation

During the hot deformation of polycrystalline alloys with low/medium stacking fault energy, new grains are formed by strain–induced grain boundary motion; this occurs once a critical shear strain γ^*_{DRX} is reached, and sufficient localised strain energy (from dislocation storage) is accummulated; further growth continues as the strain increases. A thermodynamic framework has been defined to obtain γ^*_{DRX} in terms of the deformation conditions [18, 24]:

$$\gamma^*_{DRX} = 1 - \left(1 + \frac{1}{\kappa_c}\right)\frac{T\Delta S}{\frac{1}{2}\mu b^3}, \tag{1}$$

where μ is the shear modulus, b is the Burgers vector, κ_c is a constant relating the dislocation density ρ to the average subgrain size [25]: $d_c = \frac{\kappa_c}{\sqrt{\rho}} = \frac{12\pi(1-\nu)}{(2+\nu)}\left(1 + \frac{T\Delta S}{\mu b^3}\right)\frac{1}{\sqrt{\rho}}$, where ν is the Poisson's ratio, and ΔS is the entropy accounting for dissipation effects when grain boundary bulging occurs; ΔS is associated with the possible dislocation migration paths if subgrain boundaries are formed by a dislocation arrangement [26, 24]. When $\gamma^*_{DRX} \leq 0$, then γ^*_{DRX} is fixed null. The entropy equals:

$$\Delta S = k_B \ln\left(\frac{\dot{\varepsilon}_0 + \vartheta}{\dot{\varepsilon}}\right), \tag{2}$$

where $\dot{\varepsilon}_0$ is a constant related to the critical resolved shear stress to trigger slip and the speed of sound, and it is in the range of $10^7 - 10^8$ s^{-1} [26, 25, 24]; $\vartheta = 10^{13}\exp\left(-\frac{E_m}{RT}\right)$ s^{-1} is the vacancy atomic jump frequency, and E_m is the vacancy migration energy. Details on ΔS applications can be found elsewhere [26, 27, 24, 25, 28].

The second term in equation 1 accounts for the effective stored boundary energy ($\frac{1}{2}\mu b^3$) available to trigger grain boundary motion ($T\Delta S$); this ratio also accounts for dynamic recovery effects prior to recrystallisation [24]. Following this result, the activation energy for grain nucleation Q_{nuc} during DRX is obtained by subtracting the stored energy from the

grain boundary motion energy [18]:

$$Q_{nuc} = \frac{1}{8}\left(\frac{1}{2}\mu b^3 - \left(1 + \frac{1}{\kappa_c}\right)T\Delta S\right), \tag{3}$$

where 8 is a geometric factor that accounts for the effective boundary sites where grain bulging occurs. This formulation has been applied to describe the macroscopic flow stress and the average grain size evolution during DRX in pure FCC materials and binary alloys [24, 18]. Further applications are presented in this work.

These results have also been employed to predict the stress–strain evolution of pure and multicomponent FCC materials [24, 29, 30]; this is based on describing the dislocation density once γ^*_{DRX} has been reached and dynamic recovery and recrystallisation are present. The dislocation annihilation term due to grain growth is expressed as a function of the stored boundary energy and the entropy. However, no grain size evolution or its effects on dislocation evolution were included in the analysis.

3.2 Dynamic grain size

The average grain size $\overline{D}$ at a given shear strain (γ) is computed by adding the size of each grain D_i over the total number of grains N for a sufficiently large region [18]:

$$\overline{D} = \frac{1}{N}\sum_{i=1}^{N} D_i, \tag{4}$$

where N depends on the nucleation of additional grains and $\{D_i\}$ includes both recrystallised and deformed grains. The average recrystallised grain size D_{DRX} can also be obtained when the previous summation is divided into the number N_0 of deformed grains D_j^{def} prior to recrystallisation and the number $N - N_0$ of new recrystallised grains D_k^{Rex} during straining ($\sum_{i=1}^{N} D_i = \sum_{j=1}^{N_0} D_j^{Def} + \sum_{k=N_0+1}^{N} D_k^{Rex}$). The first term equals the average deformed grain

size, whereas the second equals D_{DRX}; the mean values are with respect to the total grain population.

The evolution of the average grain size $\overline{D}$ with strain is described by differentiating the previous expression with respect to γ, and neglecting spatial contraction or expansion at the microstructural scale [31]. The evolution equation equals [18]:

$$\frac{d\overline{D}}{d\gamma} = \frac{1}{N}\frac{dN}{d\gamma}\left(D_{ss}\left(1 - \frac{N_0}{N}\right) - \overline{D}\right), \tag{5}$$

where D_{ss} is the steady state grain size and $\frac{dN}{d\gamma}$ is the grain nucleation rate. This equation is valid for $\gamma \geq \gamma^*_{DRX}$; below this value $\overline{D} = D_0$. Once D_{ss} and $\frac{dN}{d\gamma}$ are obtained, the dynamic grain size evolution follows. The former accounts for grain growth effects (see Section 3.3), whereas the latter links grain nucleation effects to the average grain size evolution.

3.3 Steady state grain size

The steady state grain size D_{ss} is reached when the net driving pressure P for grain boundary bulging disappears [32]. This is due to the fact that the grain boundary velocity of recrystallised grains is the product of the mobility and the driving pressure, where the former is always positive. D_{ss} determines the limiting condition for grain growth. In a polycrystalline superalloy, P is composed of contributions from:

1. The reduction in stored energy $P_1 = \left(\frac{1}{2}\mu b^2 \rho\right)\left(340\frac{d_c^2}{\overline{D}^2}\exp\left(-\frac{Q_{nuc}}{k_B T}\right)\right)$ where the second term represents the effective area consumed by the new grains (grain nucleation effects) [18].

2. A capillary pressure term $-P_2$ from the variation in grain boundary curvature $P_2 = \left(\frac{\chi_{GB}}{\overline{D}}\right)\left(\frac{D_{DRX}}{\overline{D}}\right)$, where χ_{GB} is the grain boundary energy and the second term accounts for the effective length where capillary effects take place, on the recrystallised grains only (grain nucleation effects).

3. A solute drag pressure term $-P_3$, resulting from solute atoms segregated around grain boundaries, reducing the stored energy available for additional motion.

4. A particle pinning term $-P_4$, stemming from small particles hindering grain growth and reducing the stored energy available for further motion.

These factors are added:

$$P = P_1 - P_2 - P_3 - P_4, \tag{6}$$

and $D_{ss} = \overline{D} = D_{DRX}$ is achieved once $P = 0$. Expressions for P_3 and P_4 in Ni–based superalloys are explored in the following section; the particle pinning term (P_4) was not introduced previously.

4 Grain structure evolution in superalloys

4.1 Solute drag

The conventional approach to solute drag in alloys [33, 32, 23] is modelled on a dilute solute atmosphere which migrates with, or breaks away from the grain boundary. In highly alloyed materials this approach is not supported by the migration rate data [34]. An alternative approach considers a binding energy between the boundary and the solute which allows a build-up of the solute on the boundary plane where it changes not only the rate of migration, but also the mechanism (as exhibited by the activation enthalpy for migration). In this way it is possible to define areas of the boundary over which the solute atoms are adsorbed onto the boundary exerting a disproportionate effect on the migration rate [32]. This approach has been proposed previously to describe solute drag P_3 during dynamic recrystallisation [18]. The drag pressure is dealt with simply as a reduction in the boundary area experiencing the full driving force and hence is set equal to a fraction p_s of the stored energy ($P_3 = p_s P_1$) required by boundaries to continue moving once solute atoms segregate around them. The

dimensionless parameter $p_s < 1$ is related to the frequency of grain boundaries encountering x_s solute atoms during recrystallisation, the distance over which they are retained in the boundary and the solute atom fraction x_s of element S. It corresponds to an exponential distribution [35]: $p_s = 1 - \exp(-\alpha_{sol} b \Lambda_s^{-1}) = 1 - \exp(-\alpha_{sol} x_s^{1/3})$, where $\alpha_{sol} b$ is the drag atmosphere and $\Lambda_s = b/x_s^{1/3}$ is the average solute spacing [36]; α_{sol} is a dimensionless constant linearly scaling with the atomic radius r_s of element S. For binary Ni alloys, α_{sol} equals [18]: $\alpha_{sol} = 562.6 r_s - 67.15$, where 562.6 (in nm^{-1}) and 67.15 are related to the boundary–solute atom binding energy in Ni. For the case of interstitial carbon atoms, $\alpha_C = 3$ was found to fit experimental measurements with good accuracy [18]. This formulation is further extended in this work to multicomponent superalloys.

In a multicomponent system containing up to seven substitutional elements and carbon (Table 1), P_3 increases as it encounters more atoms. Additional drag contributions are included in p_s:

$$p_s = 1 - \exp\left(- \sum_{s=1}^{7} \alpha_s b \Lambda_s^{-1} - \alpha_C b \Lambda_C^{-1} \right) = 1 - \exp\left(- \sum_{s=1}^{7} \alpha_s x_s^{1/3} - 3 x_C^{1/3} \right), \qquad (7)$$

where α_s is the effective drag atmosphere of element S (S=Cr, Fe, Nb, Co, Mo, Al or Ti) when other elements are also present; carbon as an interstitial is considered separately. α_s differs from α_{sol} as the presence of other elements cause variations in the solute–boundary binding energy [37, 38]. As a first approximation, α_s (in element S) is estimated by adding a correction term in the drag atmosphere of the Ni–S binary system; this correction represents the relative drag contribution of element S to the total solute concentration ($x_s / \sum_{l=1}^{7} x_l$):

$$\alpha_s = \frac{x_s}{\sum_{l=1}^{7} x_l} \alpha_{sol} = \frac{x_s}{\sum_{l=1}^{7} x_l} (562.6 r_s - 67.15). \qquad (8)$$

Additional substitutional elements can be considered. A similar decomposition has been employed to describe solute effects on the Hall–Petch relation in multicomponent Mg alloys

[39]. This modification does not include effects from solute–solute interactions, but this can be explored in further work.

4.2 Particle pinning

The presence of small particles inhibits grain boundary motion by inducing a pinning pressure on the moving boundaries [23]; the stored energy driving grain growth is thus reduced as the particle–boundary contact region is removed from the boundaries [33, 32]. The pinning pressure depends on several parameters such as particle geometry, average spacing, coherency and volume fraction [32]. This behaviour has been extensively described by the Zener pinning mechanism [23]. Although physics–based models for grain growth, including particle pinning in polycrystalline superalloys, are available [17, 40, 41, 42], their implementation during DRX is limited, as the effects of multiple distributions of particle size and the dragging of smaller particles increases the complexity considerably. Moreover, during DRX, the driving pressure stemming from the strain energy can be up to three orders of magnitude higher than the pressure due to boundary curvature [32], and up to one order of magnitude higher than the particle drag pressure [32, 33].

An alternative approach to describing particle pinning during DRX in Ni superalloys is presented: as with solute drag, the pinning term P_4 (equation 6) represents the fraction p_p of the stored energy reduced when the boundary encounters small particles randomly distributed in the material; this assumption could, in principle, also include precipitates formed at mobile grain boundaries. However, here, no specific pinning mechanism is described and only existing precipitates are considered. The fractional loss of area is determined by the particle–boundary encounter frequency, which can be approximated by an exponential distribution similar that used for solutes [35]. Let Λ_p be the average particle spacing, then

the fraction for a moving boundary to encounter a particle is:

$$p_p = 1 - \exp(-\beta_p \Lambda_p^{-1}), \tag{9}$$

where β_p is an equivalent constant length reduction in the boundary displacement when it encounters a particle. Pinning effects from $M_{23}C_6$ carbides and δ particles are considered. The particle shape of carbides is usually spherical [21, 1, 15], whereas in the δ phase often has a plate–like shape [1, 8]; this affects the average particle spacing.

The average spacing of a spherical particle ($M_{23}C_6$) is simply related to its radius $r_{M_{23}C_6}$ and volume fraction $F_{M_{23}C_6}$ [23]: $\Lambda^{-1}_{M_{23}C_6} = \frac{1}{r_{M_{23}C_6}}\left(\frac{3}{4\pi}F_{M_{23}C_6}\right)^{1/3}$. For δ particles, approximated by a square plate–like shape, an aspect ratio $h_\delta = l_\delta / r_\delta$ is defined between the length l_δ and thickness r_δ, and the average δ spacing becomes [33]: $\Lambda_\delta^{-1} = \frac{1}{l_\delta}\left(h_\delta F_\delta\right)^{1/3}$. From the definition of p_p, P_4 increases if the particle size is reduced or if the volume fraction is increased; this result is consistent with Zener theory [23]; however, rather than considering the loss of grain boundary energy, the continuous variation in the stored energy (P_1) driving grain growth is examined.

To capture the pinning effects fully the particle size and morphology need to be characterised for the test conditions. For example, the form of the δ phase in IN 718 has been extracted from Guest's work [7]: an average particle thickness of $\sim$1 μm with average length 6 μm has been found when the alloy is heat treated at 1000 °C for 3 hours. Assuming that no coarsening or additional particle nucleation takes place during deformation, an optimal value of $\beta_\delta = 7.6$ μm was fitted, resulting in $\beta_\delta \Lambda_\delta^{-1} \approx 2.3 F_\delta^{1/3}$ for these conditions. In other work, Bombac *et al.* [15] have observed $M_{23}C_6$ particles with radius ~ 0.3 μm in Nimonic 80A heat treated at 1473 K for 180 s; for this alloy an optimal value of $\beta_{M_{23}C_6} = 0.72$ μm was fitted. However, the $M_{23}C_6$ average size was not experimentally characterised in other alloys, and this value is assumed to remain constant throughout this study: $\beta_{M_{23}C_6}\Lambda^{-1}_{M_{23}C_6} \approx 1.5 F^{1/3}_{M_{23}C_6}$.

By fixing the particle size a direct comparison between δ and $M_{23}C_6$ can be made; δ displays a stronger pinning effect than $M_{23}C_6$, as $\beta_\delta > \beta_{M_{23}C_6}$. Further refinement of these parameters would require additional experimental characterisation.

The parameters p_s (equation 7) and p_p (equation 9) respectively embody the individual effects hindering grain growth. Both mechanisms compete simultaneously to reduce the overall stored energy, hence p_p and p_s should be coupled into the same distribution [43]: $p_{s+p} = 1 - \exp(-\sum_s \alpha_s x_s^{1/3} - 3x_C^{1/3} - 1.5F_{M_{23}C_6}^{1/3} - 2.3F_\delta^{1/3})$. This also implies that P_3 and P_4 in equation 6 are coupled, leading to the expression:

$$P_3 + P_4 = p_{s+p}P_1 = \left[1 - \exp\underbrace{\left(-\sum_{s=1}^{7}\alpha_s x_s^{1/3} - 3x_C^{1/3}\right)}_{\text{Solute drag}}\underbrace{-1.5F_{M_{23}C_6}^{1/3} - 2.3F_\delta^{1/3}\Big)}_{\text{Particle pinning}}\right]P_1. \quad (10)$$

Finally, the steady state grain size is obtained when equation 6 is null and $\overline{D} = D_{DRX} = D_{ss}$, resulting in [18]:

$$D_{ss} = 170\frac{\kappa_c \mu b^3}{\chi_{GB}}\underbrace{\exp\left(-\sum_{s=1}^{7}\alpha_s x_s^{1/3} - 3x_C^{1/3}\right)}_{(a)}\underbrace{\exp\left(-1.5F_{M_{23}C_6}^{1/3} - 2.3F_\delta^{1/3}\right)}_{(b)}\underbrace{\exp\left(-\frac{Q_{nuc}}{RT}\right)}_{(c)}. \quad (11)$$

This expression explicitly includes (a) solute drag, (b) particle pinning and (c) temperature and strain rate (equation 3) effects on the steady state grain size evolution (and consequently in $\overline{D}$ and D_{DRX}) in polycrystalline superalloys. It is worth noting that equation 11 is valid for the experimental conditions considered in this work, as the constants 1.5 and 2.3 in item (b) are related to the average size and aspect ratio of δ and $M_{23}C_6$ estimated for the alloys tested. In the general case, item (b) should be replaced by $\exp\left(-\frac{0.72}{r_{M_{23}C_6}}\left(\frac{3}{4\pi}F_{M_{23}C_6}\right)^{1/3} - \frac{7.6}{l_\delta}h_\delta^{1/3}F_\delta^{1/3}\right)$. The effect of particle size and shape on the recrystallised grain size are explored in the Results section.

4.3 Grain nucleation rate and dynamic grain size

The grain nucleation rate during DRX $\frac{dN}{d\gamma}$ depends on the grain population as strain evolves [44, 23]; for static recrystallisation, this value is usually fixed at a constant value [23]. However, during DRX new grains are nucleated from a continuous strain energy source, increasing the potential nucleation sites as the number of grains N increases. Following classical nucleation theory, this can be represented by an Arrhenius equation [32]:

$$\frac{dN}{d\gamma} = N \exp\left(- \frac{Q_{nuc}}{k_B T}\right), \tag{12}$$

where Q_{nuc} is the activation energy for grain nucleation (equation 3), The nucleation rate constant of 1 (strain)$^{-1}$ was fixed, and N accounts for the additional nucleation sites during straining at grain boundaries. Particle stimulated nucleation is not considered in this work [33]; however, this can be explored in a future study by incorporating an additional nucleation term, depending on the particle–boundary interactions. The average grain size evolution is finally obtained by solving the previous equation with an initial grain population N_0 and inserting this expression into equation 5. The solution is:

$$\overline{D} = \underbrace{D_0 \exp\big(- a_D(\gamma - \gamma^*_{DRX})\big)}_{(A)} + \underbrace{D_{ss}(1 - (1 + a_D(\gamma - \gamma^*_{DRX})) \exp\big(- a_D(\gamma - \gamma^*_{DRX})\big))}_{(B)}, \tag{13}$$

where $a_D = \exp\big(- \frac{Q_{nuc}}{k_B T}\big)$; $\overline{D} = D_0$ for $\gamma \leq \gamma^*_{DRX}$. Term (A) in equation 13 decreases with strain, eventually vanishing, whereas term (B) is initially null and increases with strain tending to D_{ss}. The average recrystallised grain size D_{DRX} has been found to equal term (B) [18]:

$$D_{DRX} = D_{ss}(1 - (1 + a_D(\gamma - \gamma^*_{DRX})) \exp\big(- a_D(\gamma - \gamma^*_{DRX})\big)). \tag{14}$$

An interesting aspect of this result is that the evolution of $\overline{D}$ and D_{DRX} is controlled by the activation energy for grain nucleation Q_{nuc} and the steady state grain size D_{ss} only. Initial grain size effects are shown in $\overline{D}$.

4.4 Grain size distribution evolution

Grain size statistics during normal grain growth have been well characterised [43, 32]; the resulting distributions are usually represented by standard probability distributions such as Lognormal, Weibull or Rayleigh functions [33]. However, characterising size distributions during discontinuous dynamic recrystallisation requires additional considerations [33, 7]: 1) the continuous nucleation of new grains modifies the shape of the initial distribution as the strain increases; 2) recrystallised grains grow, eventually fully consuming the deformed regions, decreasing the size of deformed grains and shifting the initial distribution towards lower values; 3) the relative contribution of the deformed grains to the statistics also decreases and eventually vanishes; 4) the significant number of small grains can give rise to an additional mode in the distribution function, leading to a bimodal function [45].

Taking these features into consideration as the strain increases, a model describing the grain size distribution $p[D]^*$ during DRX is proposed:

1. An initial size distribution is defined $p_{Def}[D]$ with average size $\overline{D}$ (equation 13); p_{Def} remains constant until DRX occurs ($\gamma \leq \gamma^*_{DRX}$);

2. once DRX begins, an additional size distribution $p_{Rex}[D]$ is introduced, containing freshly recrystallised grains only. The average size of this subset is D_{DRX} (equation 14).

3. Both distributions are mixed by a factor $f \leq 1$ that accounts for the relative number fraction of recrystallised grains being introduced into the distribution; $1 - f$ represents

*$[D]$ denotes the functional dependence of D in p, p_{Def} and p_{Rex}.

the fraction of deformed grains remaining in the material at a given strain. $f = 1$ is reached once the material is fully recrystallised and $f = 0$ if $\gamma \leq \gamma^*_{DRX}$.

4. $p_{Def}(1-f)$ decreases, eventually vanishing, whereas $p_{Rex}f$ increases, reaching a constant distribution at steady state.

The grain size distribution p during deformation is mathematically expressed as:

$$p = p_{Def}(1 - f) + p_{Rex}f. \tag{15}$$

The fraction f reflects the continuous nucleation of new grains during straining, whereas p_{Rex} describes the growth behaviour; $p_{Rex}f$ represents the fractional number of recrystallised grains in the total size distribution. This allows us to deconvolute the grain size distribution into recrystallised and deformed regions, as the nucleation and growth effects are isolated. Hence, p_{Rex} can be individually represented by a normal–growth distribution function, and f can be expressed in terms of the increase in the number of recrystallised grains. Lognormal distributions are adopted in $\overline{D}$ and D_{DRX} to simplify the calculations:

$$\begin{aligned} p_{Def}[D] &= \frac{1}{D\sqrt{2\pi}\sigma_1} \exp\left(- \frac{\left(\ln(D/\overline{D})\right)^2}{2\sigma_1^2} \right) \\ p_{Rex}[D] &= \frac{1}{D\sqrt{2\pi}\sigma_2} \exp\left(- \frac{\left(\ln(D/D_{DRX})\right)^2}{2\sigma_2^2} \right), \end{aligned} \tag{16}$$

where σ_i are in the range of $0.4 \leq \sigma_i \leq 1$ [43]; optimal constant values were respectively found to be $\sigma_1 = 0.4$ and $\sigma_2 = 0.6$ for the tested alloys. The use of similar distributions (Weibull, or Rayleigh) leads to equivalent results [43]. For the case of p_{Def}, adopting a Lognormal distribution implies that normal growth occurred during the previous heat treatment. The initial distribution can differ depending on the thermomechanical processing routines. This can be introduced in p_{Def}.

As a first approximation, the number fraction f of recrystallised grains can be approx-

imated by the ratio between the total recrystallised grain size length and the total grain length, as the microstructure evolution is usually characterised by the linear intercept method: $f = \frac{\sum_{k=N_0+1}^{N} D_{k,Rex}}{\sum_{i=1}^{N} D_i} \approx \frac{D_{DRX}}{\overline{D}}$ This is due to the lack of microstructural characterisation on the relative grain number for the materials tested. f is fixed for a given strain. Combining this result with equations 15 and 16, the grain size distribution becomes:

$$p[D] = p_{Def}[D]\left(1 - \frac{D_{DRX}}{\overline{D}}\right) + p_{Rex}[D]\left(\frac{D_{DRX}}{\overline{D}}\right). \tag{17}$$

p evolution depends on $\overline{D}$ and D_{DRX}, allowing full characterisation of the grain size distribution evolution during DRX with three equations only (13, 14 and 17). However, strong particle pinning may also cause variations in σ_i [43].

4.5 Recrystallised volume fraction

The recrystallised volume (area) fraction[†] is defined as the ratio between the area covered by recrystallised grains and the total grain area:

$$V_f = \frac{\sum_{k=N_0+1}^{N} D_{k,Rex}^2}{\sum_{i=1}^{N} D_i^2}. \tag{18}$$

The previous equation can be expressed in terms of $p[D]$ and $p_{Rex}[D]f$ by computing the second moment of the respective distribution [35]. If the continuum distributions in equation 16 are discretised, the volume fraction equals:

$$V_f = \frac{\sum_{k=N_0+1}^{N} D_{k,Rex}^2}{\sum_{i=1}^{N} D_i^2} \approx \frac{\int_0^\infty D^2 p_{Rex}[D] f dD}{\int_0^\infty D^2 p[D] dD} \approx \frac{\sum_{i=1}^{N_g} D_k^2 p_{Rex}[D_i] f \Delta D_i}{\sum_{i=1}^{N_g} D_i^2 p[D_i] \Delta D_i}, \tag{19}$$

[†]Microstructure characterisation is estimated from two dimensional micrographs, hence the experimental volume fraction describes the total recrystallised area fraction.

where ΔD_i is the grain size interval from the distribution discretisation [35], and N_g is the number of grain intervals from the discretisation. This expression allows us to estimate the recrystallised volume fraction without the introduction of additional constitutive relations, as it only depends on the grain size distribution. This also implies that V_f only depends on $\overline{D}$ and D_{DRX}.

4.6 Grain number density

The grain number density $\hat{N}$ is obtained by computing the ratio between the total grain number N and grain area. If circular grains are assumed, the grain area equals $\frac{\pi}{4}\sum_i D_i^2$. As with V_f, the previous summation can be expressed in terms of $p[D]$; $\hat{N}$ becomes:

$$\hat{N} = \frac{\pi}{2}\frac{N}{\frac{\pi}{4}\sum_i D_i^2} \approx \frac{2}{\sum_{i=1}^{N_g} D_i^2 p[D_i]\Delta D_i}, \tag{20}$$

where $\frac{\pi}{2}$ is a stereological correction factor from grain size measurements by the linear intercept method [46].

5 Results

The model results are tested against experimental measurements in 11 superalloys (Table 1). Where physical parameters employed in the model were not available for the specific alloys they were taken equal to those for pure Ni: χ_{GB}=0.8 J m^{-2} [33], $b = 0.249$ nm [47], $E_m = 1.1$ eV [24], and $\nu = 0.32$ [47]. $\dot{\varepsilon}_0 = 5 \times 10^7$ s^{-1} is considered constant for all alloys [24]. Table 3 shows the shear modulus values for the alloys tested; these values were obtained from [48] and converted to analytical expressions to capture their temperature variation and simplify calculation. In the case of the 625 series, μ was taken equal to IN 625, as their individual temperature variations were not found in the literature; the shear modulus of AllVac718 was

also considered equal to Inconel 718, as the chemical composition of these alloys is almost identical. For the 4 Nimonic alloys μ showed similar values in.[48].

Table 3: Shear modulus variation with temperature (in K) for the tested superalloys.

Alloy	μ (GPa)
AllVac 718	$82.38 - 0.015T - 5.5 \times 10^{-6}T^2$
IN 625, Age 625, Pyromet 625	$83.52 - 0.017T - 5 \times 10^{-6}T^2$
IN 690	$82.76 - 0.0085T - 1.4 \times 10^{-5}T^2$
IN 718	$82.38 - 0.015T - 5.5 \times 10^{-6}T^2$
IN 740H	$87.39 - 0.009T - 1.42 \times 10^{-5}T^2$
Nimonic 75, 80A, 90, 105	$57.947 + 0.0.6T - 4.7 \times 10^{-5}T^2$

Figures 1(a),(b) show the average grain size predictions when solute drag alone is present in AllVac 718, IN Age 625, 718, 740H and Nimonic 90; the deformation temperatures in IN 740H are above the solvus temperature. In all cases, the results are expressed in terms of the axial strain $\varepsilon = \gamma/M$, where M is the Taylor orientation factor in FCC alloys and has a value of 3 [24]. Figure 1(a) shows the comparison between the model and experimental measurements at various deformation conditions (Table 2), and Figure 1(b) shows the comparison at various temperatures; the data sets for IN 718 in Figure 1(a) and (b) were obtained from [11, 10] and [12], respectively. The model predictions and experimental measurements display similar values in most cases. However, in Figure 1(a) there are considerable variations in fine–grained Allvac 718, IN Age 625 and coarser grained IN 718 with D_0=54 μm; these discrepancies could be due to metadynamic recrystallisation occurring during cooling to room temperature, as the model predicts finer grains in all cases. Figures 1(c),(d) compare the average grain size predictions with experimental measurements when additional $M_{23}C_6$ pinning is introduced. Figure 1(c) shows IN 740H and Nimonic 80A at various deformation

conditions outlined in (Table 2); Figure 1(d) shows $\overline{D}$ variations with temperature for IN 690 and Nimonic 75 and 105. These figures also show drag effects for deformation conditions above the $M_{23}C_6$ solvus temperatures. The atom fraction of elements forming $M_{23}C_6$ (as is the case for δ in the following results) was subtracted to estimate the effective solute drag rate; this fraction was obtained from Thermocalc. The model shows good agreement with most experimental measurements. However, 3 measurements in Nimonic 80A display lower values with respect to the model predictions, these correspond to specimen deformation at 1223 K [15], and a coarser grain size predicted for IN 690 at 1473 K. These discrepancies could be due to particle size variations between testing conditions since this was not reported and single size was assumed in the model.

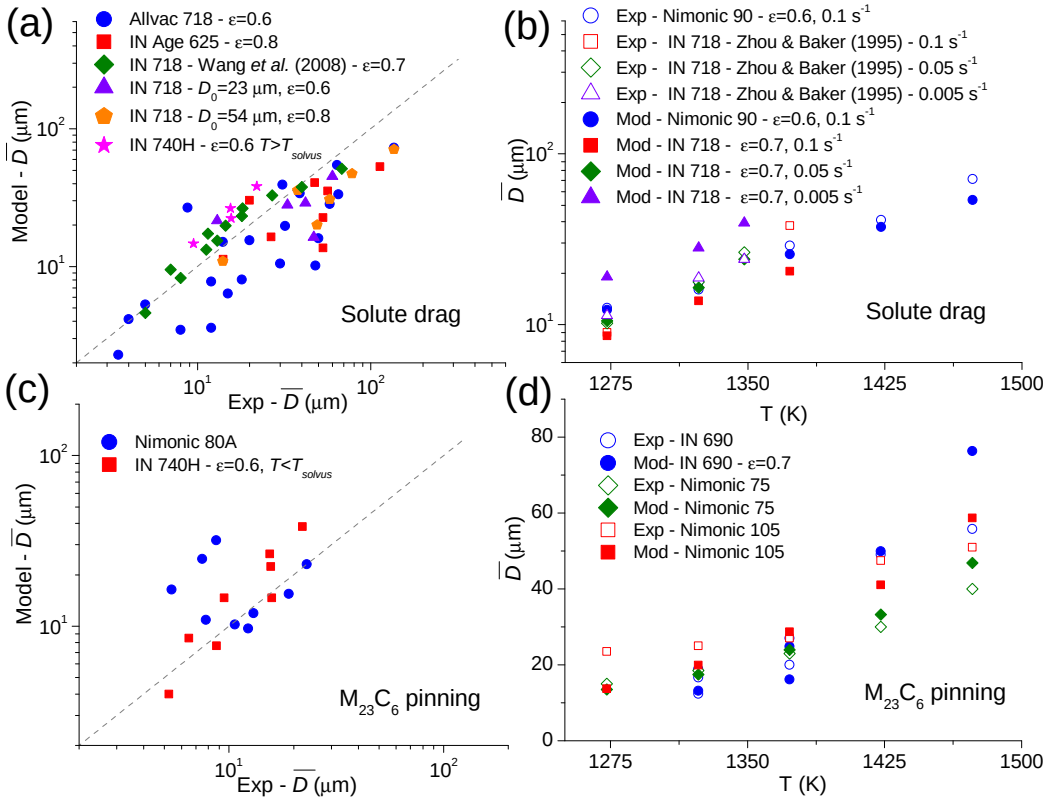

Figure 1: Average grain size variation when solute drag effects are included (a),(b) and additionally with $M_{23}C_6$ pinning (c),(d). T_{solvus} for IN 740H and 690 are ≈1380 and 1440 K, respectively.

Figures 2(a),(b) show the variations in $\overline{D}$ with strain (ε = 0.1, 0.5 and 1.2) for various deformation conditions and these results are compared against experimental measurements for IN 718; no precipitates were present [9]. Figure 2(a) shows the measured data for various temperatures and at strain rates 0.001, 0.01, 0.1 and 1 s^{-1}; Figure 2(b) shows the variation in $\overline{D}$ with strain at different temperatures and a strain rate of 1 s^{-1}. As no initial grain sizes were provided, these were fitted to match the first experimental measurement at $\varepsilon = 0.1$ [9]. The model shows good agreement for the conditions tested. Figures 2(c),(d) show the grain number density predictions compared with the experimental measurements in IN 718; the experimental data were extracted from [7]. These results are inversely related to the average grain size (equation 20). Data displayed in Figures 2(c),(d), 3 and 4(a),(b) corresponds to the same set of experiments; a complete characterisation linking the grain density (grain size), size distribution and recrystallised volume fraction is available from these results. Figure 2(c) and (d) show the model results when δ pinning (c) and when solute drag alone (d) are present at higher temperatures (Table 2). In both cases, the model shows good agreement at low strain rates, however, considerable discrepancies are apparent at higher strain rates and ε = 0.8 in (c), and at 1.1 s^{-1} and $\varepsilon > 0.4$ in (d). Such variations could be due to a lower recrystallised volume fraction leading to localised variations in the grain size, whereas at lower strain rates, a more homogeneous microstructure is expected.

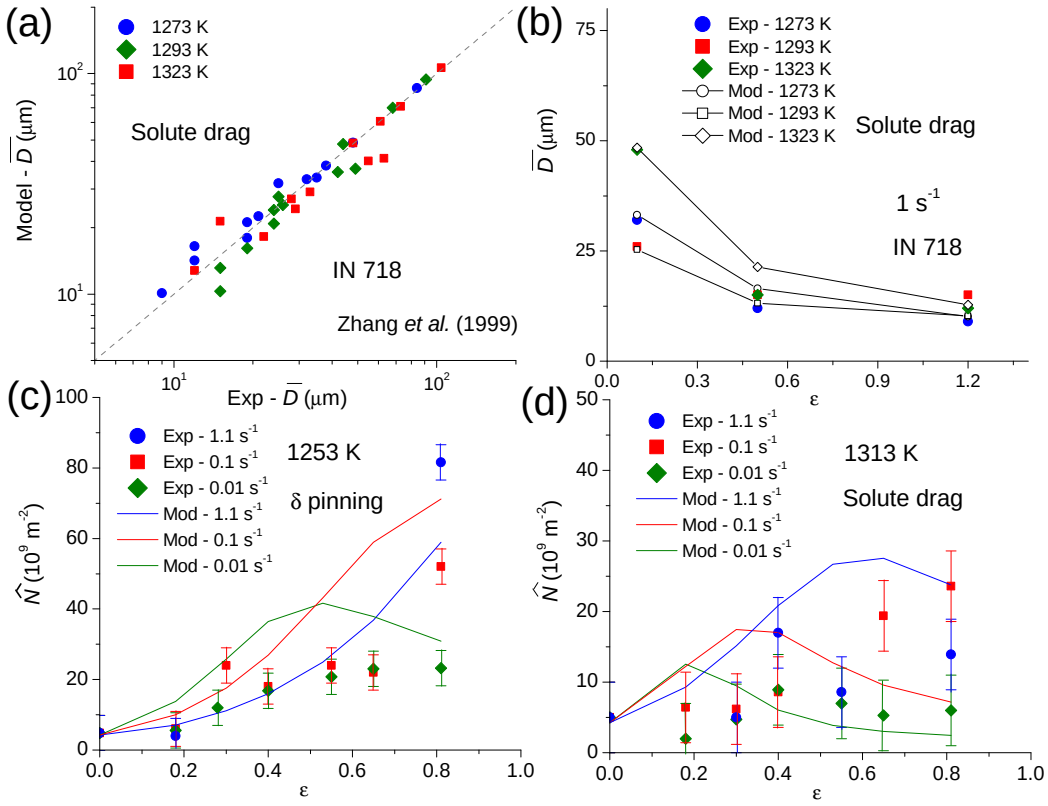

Figure 2: (a),(b) Average grain size variation, and (c), (d) grain number density variation with strain in IN 718 at various deformation conditions.

Figure 3 shows the grain size distributions in IN 718 at various strains when the specimen is deformed at 1313 K and 0.45 s^{-1} [7]; only solute drag is present at these conditions; $\overline{D}$ and D_{DRX} in equation 17 are computed with the grain size predictions (equations 13 and 14). The dashed (red) and dotted (blue) lines represent the recrystallised and deformed grain size distributions, respectively. The model shows good agreement in (a), (c) and (d); however in (b), a higher contribution is predicted from the deformed grains (hence, a lower recrystallised volume fraction). Figure 3(a) displays a bimodal distribution due to the high number of recrystallised grains; as strain increases, the contribution from deformed grains (p_{Def}) decreases, eventually being overtaken by dislocation–free grains (b),(c),(d) and vanishing once the material has fully recrystallised. This result confirms that it is possible to deconvolute the contributions from recrystallised and deformed grains in the grain size distribution.

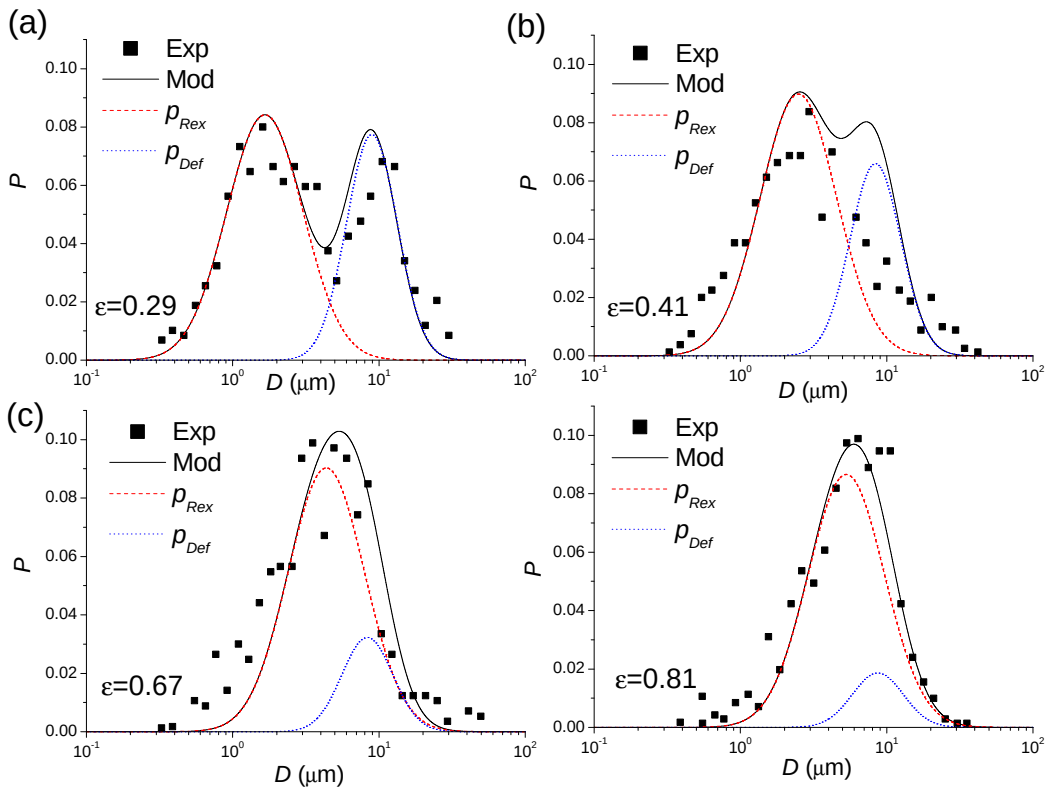

Figure 3: Grain size distribution evolution in IN 718 deformed at 1313 K and 0.45 s^{-1}.

Figures 4(a-c) show the predictions for recrystallised volume fraction (equation 19) compared with experimental measurements in IN 718 for various conditions; δ pinning is present below the solvus temperature (dashed line in (c)); experimental data in (a),(b) and (c) were extracted from [7] and [8], respectively. The same δ size (β_δ value) is assumed in (c), as no mean particle size was provided; additionally, 0.04 (wt%) of carbon is added to this alloy in (c). The minimum and maximum grain sizes for computing the summations in the volume fraction, equation 19, were 0.001 and 200 μm, respectively; a very fine grain size interval $\Delta D_i = 0.001$ μm was fixed, giving the number of intervals $N_g = 200,000$; these parameters were considered to ensure minimum errors during the numerical integration. In (a) and (b), the model shows good agreement at 1313 K, and at 1253 K at lower strain rates (0.01 s^{-1}). However, at 1253 K a lower recrystallised volume fraction is predicted at higher strain rates (except at $\varepsilon = 0.8$). This discrepancy could be due the omission of the σ_i variation (σ_i char-

acterises the dispersion in the size distribution functions in equation 17) when precipitates are present and modify the size distribution shape. The model also shows good agreement for all conditions in (c), except for 1293 K at 0.01 s^{-1} and 1350 K at 1 s^{-1}; in the former, a higher δ volume fraction or finer particle size could be present in the experiments (despite T being close to T_{solvus} [21]), whereas in the latter, metadynamic recrystallisation following deformation could be occurring. Figure 4(d) shows the model predictions for the average recrystallised grain size D_{DRX} and its respective volume fraction variation in IN 625 for various temperatures. The model shows good agreement, capturing the recrystallised grain size and volume fraction evolution, except for D_{DRX} at temperatures above 1400 K; again these discrepancies could be due to possible metadynamic recrystallisation occurring after deformation, as higher boundary migration rates occur at higher temperatures.

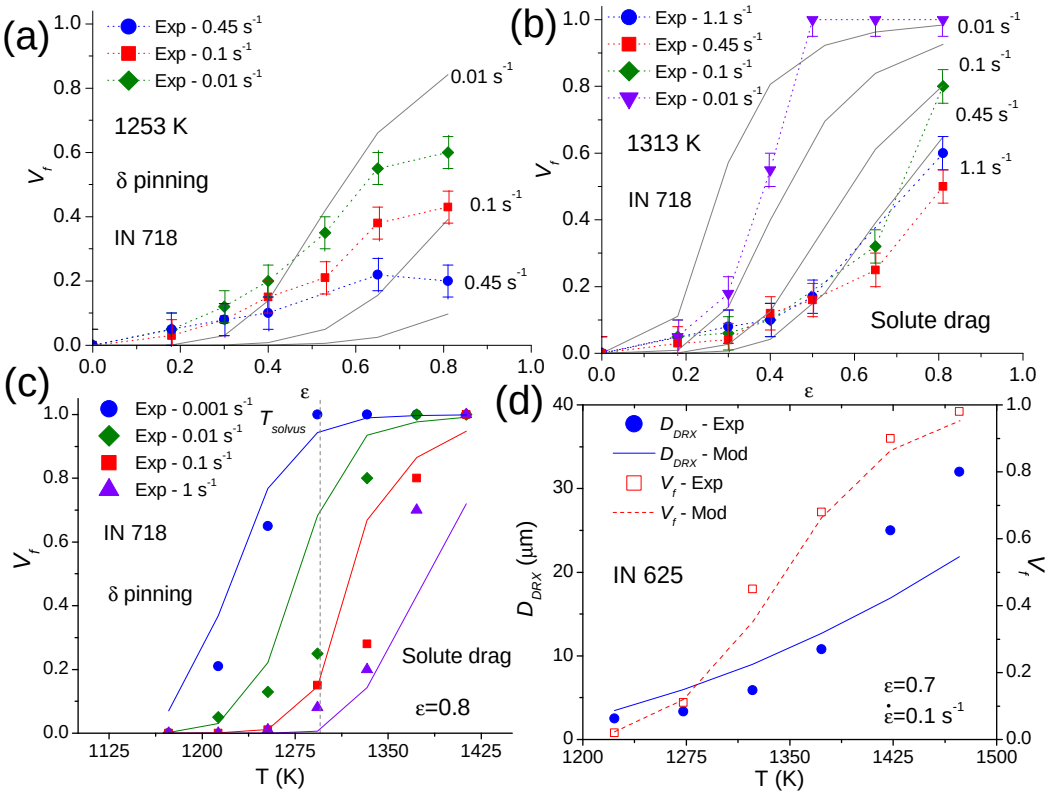

Figure 4: (a), (b), (c) Volume fraction variation in a IN 718 superalloy for various deformation conditions. (d) Recrystallised grain size and volume fraction variation in IN 625.

To illustrate how this model can be employed to predict microstructure evolution under different processing routines we focus on IN718. Figure 5 shows the recrystallised volume fraction and recrystallised grain size evolution using the same data as Figure 4(c), but here Figures 5(a) and (b) respectively show V_f and D_{DRX} variations when particle pinning is present from a previous heat treatment (solid lines), and when only solute drag is present (dotted lines). At 1213 K and 0.001 s^{-1}, the volume fraction increases by ∼30 % when δ is inhibited, whereas at 1293 K, V_f increases by ∼ 2 % only; in both cases, the recrystallised grain size also increases from 5 to 10 μm at 1213 K, and from 20 to 30 μm at 1293 K.

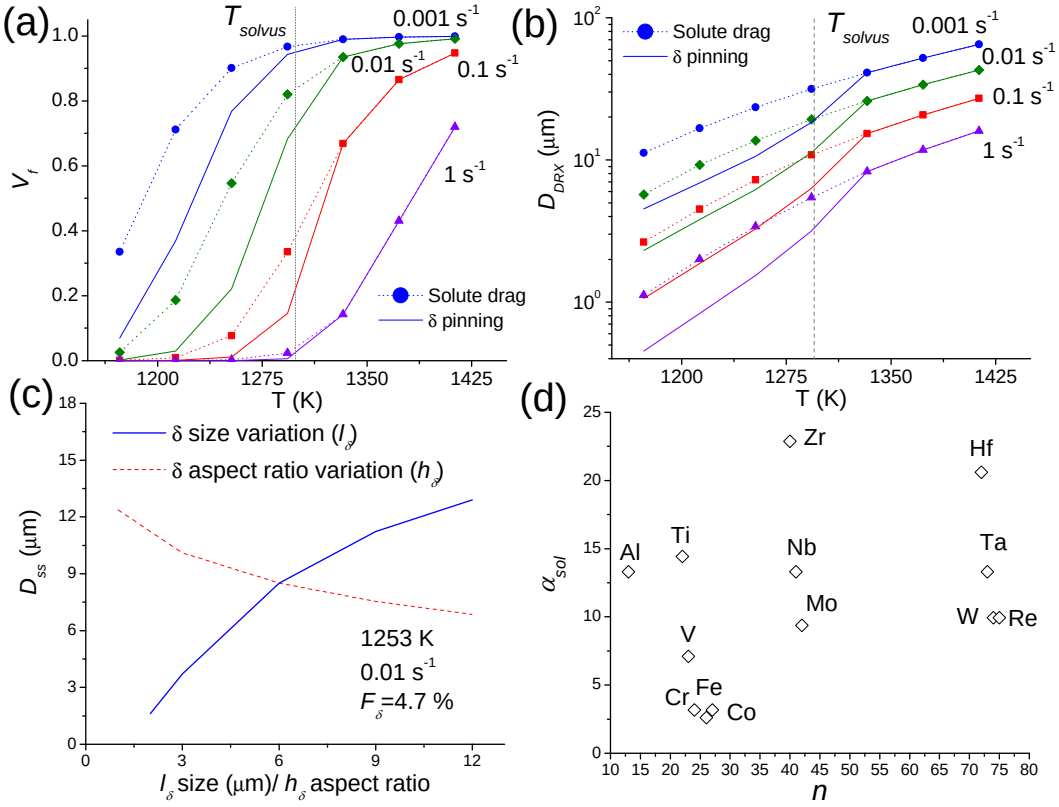

Figure 5: (a),(b) Comparison between particle pinning and pure solute drag in IN 718 at various deformation conditions. (c) Steady state grain size variation with particle size and shape. (d) Solute drag atmosphere in several substitutional elements.

Extending the analysis to the general cases when the δ size and aspect ratio are no longer fixed, Figure 5(c) shows the influence of δ size (solid line) and shape (dashed line) on the

steady state grain size at 1253 K (Section 4.2); material conditions are taken from Guest's results; δ volume fraction is fixed for the given temperature (Table 2). The size variation is estimated by fixing the particle aspect ratio ($h_\delta = 6$) for different δ lengths (l_δ), whereas the shape variation is computed with a fixed particle size ($l_\delta = 6$ μm) for different h_δ; both variations are possible under different treatments. The model schematically predicts a strong variation in size, a finer grain size is achieved as the δ size is decreased; on the other hand, the influence of aspect ratio variation is weaker, a finer grain size is predicted as the aspect ratio increases. These results are in agreement with classical particle pinning approaches [33]; however more detailed experimental characterisation is required to validate these predictions. Finally, the solute drag atmosphere is compared for the various elements commonly added to polycrystalline superalloys; elements with high α_{sol} values induce a higher drag effect (equation 8). Figure 5(d) shows α_{sol} values in 13 substitutional elements; the horizontal axis is shown in terms of solute atomic number. Hf and Zr display the highest drag atmosphere, hence a finer grain structure can be achieved when these elements are added, whereas Fe, Cr and Co have the weakest influence on grain refinement. Al, Ti, Nb and Ta display similar intermediate drag effects. These results can be used to optimise material processing routes during alloy development.

6 Discussion

This work presents a novel approach to describe grain structure evolution during dynamic recrystallisation in Ni–based superalloys; it predicts average and recrystallised grain size, grain size distribution, number density and volume fraction variations with strain. Evolution equations for the average grain size $\overline{D}$ and recrystallised grain size D_{DRX} were obtained in previous work; they both depend on the grain nucleation rate and steady state grain size. A nucleation rate depending on the grain population was postulated in Ni–based superalloys.

The steady state grain size was obtained when the net driving pressure for grain growth was null; this included contributions from the stored energy, grain curvature, solute drag and particle pinning. It was proposed that the grain size distribution p during deformation was formed by a mixed distribution of dislocation–free grains p_{Rex} and the initial size distribution p_{Def}; in both cases, lognormal distributions were adopted. This approach was corroborated with experimental observations of bimodal distributions. The recrystallised volume fraction V_f was estimated by deconvoluting the size distribution into the area covered by recrystallised grains (p_{Def}). Both p and V_f depend on $\overline{D}$ and D_{DRX}.

An alternative approach describing the combined effects of solute drag and particle pinning on grain growth has been introduced; this is based on estimating the encounter frequency of moving boundaries with the respective mechanisms; the drag pressure is computed as the fraction (depending on the encounter frequency) of the stored energy required to overcome such obstacles. In the case of particle pinning, this is shown to depend on the average precipitate spacing, volume fraction and size. This result was simplified by fixing a constant particle size. For solutes Figure 5(d) depicts the drag intensity of each alloying element. Zr and Hf display the highest drag atmosphere. However, experimental validation is required to corroborate these results. Also, the model may be modified for materials containing particles with higher volume fraction.

The model results are applied to predict grain structure behaviour in 11 superalloys during dynamic recrystallisation, spanning wide ranges in chemistry, deformation conditions and initial microstructure. It is not only able to describe the trends, but the model also reproduces the experimental values with good accuracy. Seven substitutional elements and carbon effects were considered for solute drag refinement, and $M_{23}C_6$ and δ pinning were studied in different superalloys. Additional substitutional elements and precipitates could readily be included in this model. Moreover, the model features are not restricted to Ni alloys and could be applied to other FCC alloys such as Al, Cu and Fe (in austenitic phase),

by identifying the respective solute drag and particle pinning parameters [18].

A number of assumptions introduced in the model were required as full microstructure characterisation was not reported, such as lacking initial grain size or particle volume fraction measurements. The model discrepancies can be mainly caused by not including other mechanisms being present in the experiments. A better version of the model would require further experimental characterisation in the particular cases where the grain size is over predicted, due to the lack of particle size and localised volume fraction characterisation, and when it is under predicted due to possible metadynamic recrystallisation. For instance, the number fraction of recrystallised grains f was approximated by the ratio between the mean recrystallised grain and the mean grain size ($D_{DRX}/\overline{D}$); this accommodates characterisation of recrystallised grain fraction by a linear intercept method; however, in some cases, the grain diameter is derived from the mean root square area, in which case f could be approximated by $\left(D_{DRX}/\overline{D}\right)^2$. Another issue that arises is the method used to distinguish recrystallised grains during characterisation: in several cases this relies upon the size and location of the grains rather than any measure of the degree of deformation. Recent advances, for instance in the use of EBSD to characterise datasets, allow for a more objective approach.

The necessary assumptions of a fixed particle size and ignoring volume fraction variations other than with temperature, appears to have been a reasonable approximation. As detailed information on $M_{23}C_6$ and δ morphology in the recrystallised microstructure is limited, additional experimental characterisation would be needed to overcome these simplifications. Nevertheless, the validation of the model in IN 718 using Guest's work [7] shows a good correlation for δ. This is demonstrated in Figures 2(c)(d), 3 and 4(a),(b). In addition, it is shown in Figure 5(c) how δ size and aspect ratio variations are expected to influence the recrystallised grain size: a finer structure is achieved as δ is refined or the particle aspect ratio is increased. However these predictions need validation. Furthermore, this methodology could be combined with precipitation kinetics models to incorporate continuous precipitation

during superalloy hot forming.

An important result from this work is that the recrystallised volume fraction is shown to depend on the mean grain size once the size distribution function is identified; no additional constitutive relations are required. Moreover, this methodology can potentially be applied to describe the volume fraction evolution in metadynamic and static recrystallisation if normal growth laws are considered instead; classical approaches such as the Avrami equation [33], and its respective parameter identification would not be needed. This will be considered in future work.

Several authors have derived power–law empirical equations estimating D_{DRX} in terms of the Zener–Hollomon parameter $Z = \dot{\varepsilon} \exp\left(\frac{Q_Z}{RT}\right)$, where Q_Z is an apparent activation energy, depending on alloy's composition:

$$D_{DRX} = AZ^{-n} = A(\dot{\varepsilon})^{-n} \exp\left(-\frac{nQ_Z}{RT}\right), \tag{21}$$

where A is a constant. Table 4 shows the reported values of A, n and Q_Z in three superalloys, the original reference, and the respective deformation conditions. A in Inconel 690 and Nimonic 80A was chosen to fit the experimental grain size in [6] and [15], respectively, as this value was not reported; it is worth noting that $M_{23}C_6$ carbides are present in Nimonic 80A. Figure 6 shows our model predictions (equation 14) and D_{DRX} values employing equation 21 for these alloys. Our model predicts values very close to those from these empirical expressions; (comparison with experimental measurements is shown in Figures 1(c) and (d)). A key limitation for empirical models is that the fitting parameters can differ with the deformation range. Moreover, parameter variations, such as the recrystallised volume fraction V_f, are also reflected in the microstructure predictions. For instance, Shen *et al.* [49] have found in Waspaloy that n in equation 21 can change dramatically under the influence of particle pinning, obtaining n values of 0.16 and 0.0456 for temperatures above and below γ'–

solvus, respectively. In addition, by expressing the recrystallised volume fraction evolution in terms of an Avrami–type equation [49]: $V_f = 1 - \exp\big(-\ln(2)\big(\frac{\varepsilon}{\varepsilon_c}\big)^m\big)$, where $\varepsilon_c = D_0^{n_1} Z^{n_2}$ is a reference strain and m is a constant, they have also identified that n_1, n_2 and m display three set of values: 1) at temperatures above γ'–solvus, 2) at temperatures below and close to γ'–solvus, where small pinning occurs, and 3) at low temperatures where γ' pinning is strong [49]. This is not necessary in our model, as this transition is inherited by V_f via D_{DRX} and $\overline{D}$ (equation 19). Another example relates to the parameter n, this controls variations in the D_{DRX} with $\dot{\varepsilon}$ in equation 21, giving values in the range 0.22–0.28 (at high strains). In our model, by combining the activation energy for grain nucleation (equation 3) with the steady state grain size D_{ss} (equation 11), and neglecting the $1/\kappa_c$ term in $T\Delta S$ ($\kappa_c \geq 20$), it can be shown that the steady state grain size scales with $\dot{\varepsilon}$ as: $D_{ss} \propto (\dot{\varepsilon})^{-n}$, giving $n = 0.25$, our model can successfully recover the power–law dependence of $\dot{\varepsilon}$ on the steady state grain size. A similar analysis can be performed to relate Q_Z with alloy composition, deformation temperature and initial microstructure.

Table 4: A, Q_Z and n values for three superalloys and their application range.

Alloy	Ref.	A (μm)	Q_Z (kJ/mol)	n	T (K)	$\dot{\varepsilon}$ (s^{-1})	D_0 (μm)	ε
Inconel 718	[10]	3×10^5	443	0.27	1223-1373	10^{-3}-0.1	176	0.7
Inconel 690	[6]	2.6×10^4	380	0.22	1323-1473	0.1-1	42	0.7
Nimonic 80A	[15]	5×10^4	379	0.28	1223-1393	0.1-5	90	0.9

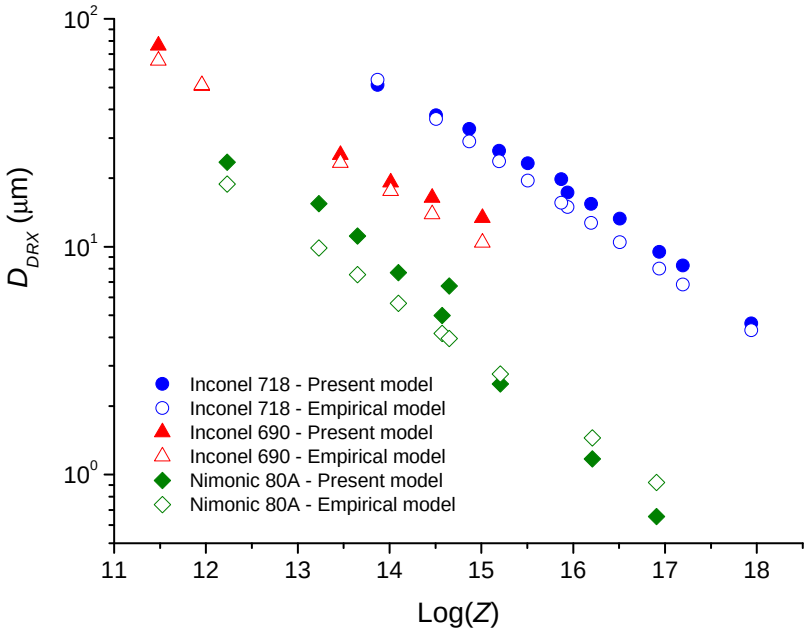

Figure 6: Grain size predictions employing the present model and by empirical fitting in IN 718, 690 and Nimonic 80A.

7 Conclusions

A new theory has been defined to predict a number of microstructure characteristics during discontinuous dynamic recrystallisation and has been validated with results from 11 Ni–based superalloys:

- dynamic, recrystallised and steady state grain size, including grain density;
- grain size distribution evolution with strain;
- and dynamic recrystallised volume fraction evolution with strain.

It has been demonstrated that the grain structure can be fully controlled by the average and recrystallised grain size values once the size distribution functions have been identified; it was also confirmed that individual contributions of the recrystallised and deformed grains

can be isolated from the overall grain behaviour during DRX. Solute drag and particle pinning ($M_{23}C_6$ carbides and intermetallic δ) effects on grain growth have been simultaneously described for a wide range of deformation conditions and composition. In principle, the model is able to capture particle size and shape effects during recrystallisation.

Acknowledgements

The authors would like to acknowledge the EPSRC, Grant numbers EP/H022309/1, EP/H500375/1 and Rolls-Royce plc. for funding and Prof. Mark Blamire of the Department of Materials Science and Metallurgy, University of Cambridge for provision of facilities.

References

[1] M. Donachie, S. Donachie, Superalloys: A technical guide, ASM International, 2002.

[2] R. Reed, The superalloys: Fundamentals and applications, Cambridge University Press, 2006.

[3] P. Chaudhury, D. Zhao, Atlas of formability AllVac 718. National Center for Excellence in Metalworking Technology (1992) 70.

[4] Q. Guo, D. Li, S. Guo, H. Peng, J. Hu, J. Nuc. Mater. 414 (2011) 440–450.

[5] D. Zhao, P. Chaudhury, R. Frank, L. Jackman, Superalloys 718, 625, 706 and Various Derivatives (1994) 315–329.

[6] S. Guo, D. Li, H. Pen, Q. Guo, J. Hu, J. Nuc. Mater. 410 (2011) 52–58.

[7] R. Guest, Ph.D. thesis, University of Cambridge (2005).

[8] H. Yuan, W. Liu, Mater. Sci. Eng. A 408 (2005) 281–289.

[9] J. Zhang, Z. Gao, J. Zhuang, Z. Zhong, Metall. Mater. Trans. A 30 (1999) 2701–2712.

[10] Y. Wang, W. Shao, L. Zhen, L. Yang, X. Zhang, Mater. Sci. Eng. A 497 (2008) 479–486.

[11] D. Zhao, P. Chaudhury, Superalloys 718, 625, 706 and Various Derivatives (1994) 303–313.

[12] L. Zhou, T. Baker, Mater. Sci. Eng. A 196 (1995) 89–95.

[13] J. Wang, J. Dong, M. Zhang, X. Xie, Mater. Sci. Eng. A 566 (2013) 61–70.

[14] N. Srinivasan, Y. Prasad, J. Mater. Process. Technol. 51 (1995) 171–192.

[15] D. Bombac, M. Brojan, M. Tercelj, R. Turk, Mater. Manuf. Processes 24 (2009) 644–648.

[16] S. Mitsche, C. Sommitsch, D. Huber, M. Stockinger, P. Poelt, Mater. Sci. Eng. A 528 (2011) 3754–3760.

[17] K. Song, M. Aindow, Mater. Sci. Eng. A 479 (2008) 365–372.

[18] E. Galindo-Nava, P. Rivera-Díaz-del-Castillo, Scripta Mater. 72 (2014) 1–4.

[19] L. Ferrer, B. Pieraggi, J. Uginet, Superalloys 718, 625 and various derivatives, TMS-AIME, 1991.

[20] W. Voice, R. Faulkner, Metall. Trans. A 16 (1985) 511–520.

[21] B. Tian, C. Lind, O. Paris, Mater. Sci. Eng. A 358 (2003) 44–51.

[22] A. Oradei–Basile, J. Radavich, Superalloys 718, 625 and various derivatives, TMS-AIME, 1991.

[23] J. Martin, R. Doherty, B. Cantor, Stability of microstructure in metallic systems, Cambridge University Press, 1997.

[24] E. Galindo-Nava, P. Rivera-Díaz-del-Castillo, Int. J. Plas. 47 (2013) 202–221.

[25] E. Galindo-Nava, P. Rivera-Díaz-del-Castillo, Acta Mater. 60 (2012) 4370–4378.

[26] E. Galindo-Nava, J. Sietsma, P. Rivera-Díaz-del-Castillo, Acta Mater. 60 (2012) 2615–2624.

[27] E. Galindo-Nava, P. Rivera-Díaz-del-Castillo, Mater. Sci. Eng. A 543 (2012) 110–116.

[28] E. Galindo-Nava, P. Rivera-Díaz-del-Castillo, Int. J. Plas. 55 (2014) 25–42.

[29] E. Galindo-Nava, P. Rivera-Díaz-del-Castillo, Mater. Sci. Forum 753 (2013) 153–156.

[30] P. Rivera-Díaz-del-Castillo, E. Galindo-Nava, Mater. Sci. Forum 753 (2013) 427–430.

[31] F. Montheillet, O. Lurdos, G. Damamme, Acta Mater. 57 (2009) 1602–1612.

[32] G. Gottstein, L. Shvindlerman, Grain boundary migration in metals, CRC Press, 2010.

[33] F. Humphreys, M. Hatherly, Recrystallization and related annealing phenomena, Elsevier, 2004.

[34] Y. Huang, H. F.J., Mater. Chem. Phys. 132 (2012) 166–174.

[35] E. Jaynes, Probability theory: The logic of science, Cambridge University Press, 2003.

[36] D. Hull, D. Bacon, Introduction to dislocations, Butterworth-Heinemann, 1999.

[37] H. Fletcher, A. Garratt-Reed, H. Aaronson, G. Purdy, W. Reynolds, G. Smith, Scripta Mater. 45 (2001) 561–567.

[38] H. Aaronson, W. Reynolds, G. Purdy, Metall. Mater. Trans. A 35 (2004) 1187–1210.

[39] I. Toda-Caraballo, E. Galindo-Nava, P. Rivera-Díaz-del-Castillo, Acta Mater. 75 (2014) 287–296.

[40] H. Jeong, J. Cho, H. Park, J. Mater. Process. Technol. 162 (2005) 504–511.

[41] D. Collins, B. Conduit, H. Stone, M. Hardy, G. Conduit, R. Mitchell, Acta Mater. 61 (2013) 3378–3391.

[42] A. Agnoli, N. Bozzolo, R. Logé, J. Franchet, J. Laigo, M. Bernacki, Comp. Mater. Sci. 89 (2014) 233–241.

[43] I. Toda-Caraballo, C. Capdevila, G. Pimentel, C. De Andrés, Comp. Mater. Sci. 68 (2013) 95–106.

[44] D. Porter, K. Easterling, Phase transformations in Metals and Alloys, CRC Press, 2009.

[45] J. del Valle, O. Ruano, Mater. Letters 62 (2008) 3391–3394.

[46] L. Chang, H. Bhadeshia, Mater. Sci. Tech. 11 (1995) 874–881.

[47] D. Lide, CRC Handbook of Chemistry and Physics, CRC Press, 2008.

[48] http://www.specialmetals.com (2013).

[49] G. Shen, S. Semiatin, R. Shivpuri, Metall. Mater. Trans. A 26 (1975) 1795–1803.